MSDE

Molecular Systems Design & Engineering

rsc.li/molecular-engineering

ROYAL SOCIETY
OF CHEMISTRY
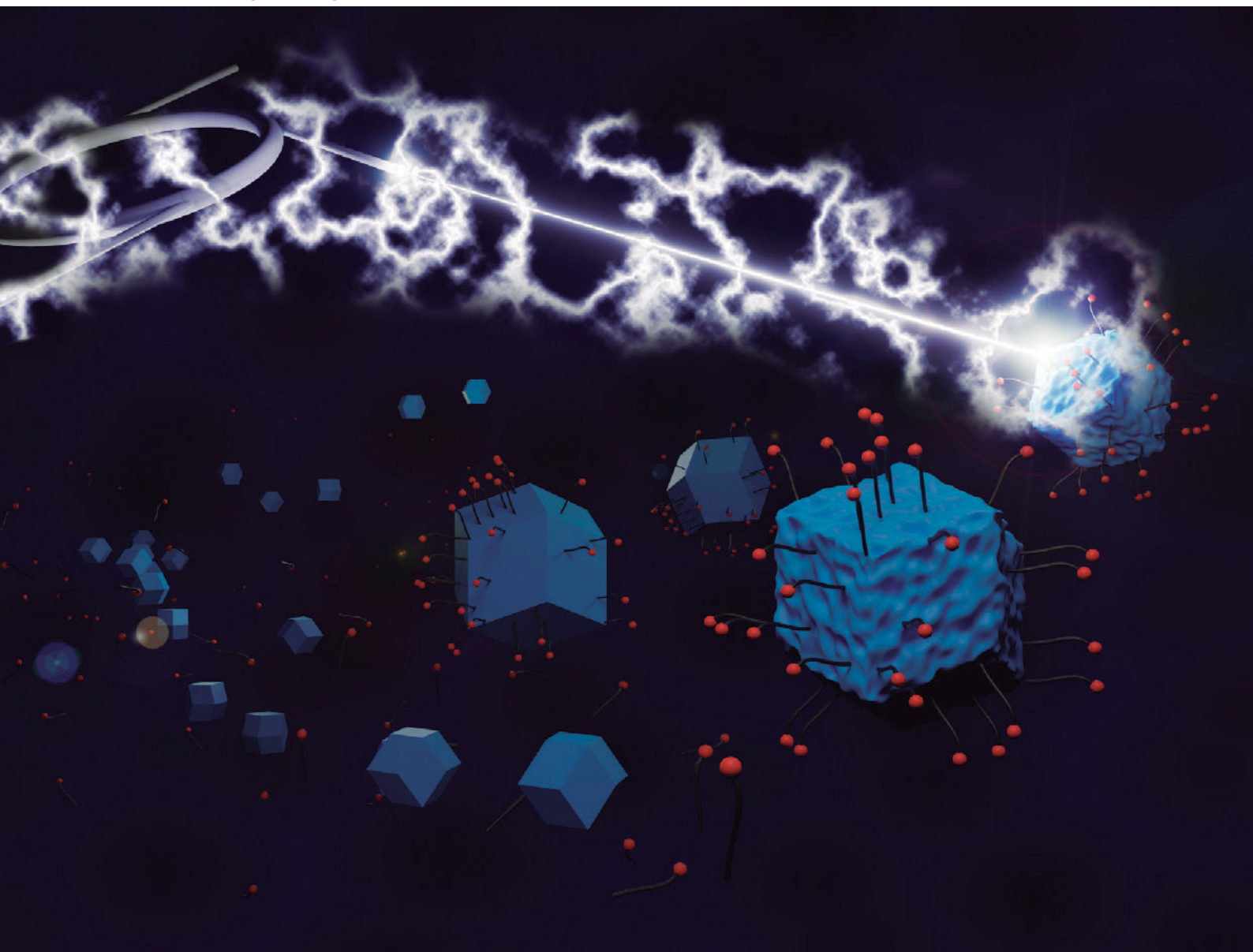
PAPER
Matías Rafti *et al.*
Post-synthetic modification and chemical modulation
of the ZIF-8 MOF using 3-mercaptopropionic acid (MPA):
a multi-technique study on thermodynamic and kinetic aspects

IChemE ADVANCING
CHEMICAL
ENGINEERING
WORLDWIDE

MSDE

ROYAL SOCIETY OF CHEMISTRY

PAPER

Check for updates

Post-synthetic modification and chemical modulation of the ZIF-8 MOF using 3-mercaptopropionic acid (MPA): a multi-technique study on thermodynamic and kinetic aspects†

Gustavo M. Segovia,[a] Juan A. Allegretto, [iD][a] Jimena S. Tuninetti,[a] Lucía B. Pizarro, [iD][a] Agustín S. Picco,[a] Marcelo Ceolín,[a] Tanja Ursula Lüdtke,[b] Elisa Bindini,[b] Desiré Di Silvio,[b] Sergio E. Moya, [iD][b] Omar Azzaroni [iD][a] and Matías Rafti [iD]*[a]

We hereby report on the thermodynamic and kinetic aspects of ZIF-8 MOF synthesis when performed using methanolic solutions of precursors and 3-mercaptopropionic acid (MPA) acting as a chemical modifying agent. MPA is of great interest as it allows us to gain control over the surface chemistry, shape, and size of colloidal porous nanounits formed. In particular, small and wide-angle X-ray scattering (SAXS/WAXS), and electron microscopy were employed for determination of suitable MPA : MeImH modification molar ratios for two different approaches: post-synthesis modification (PSM) and coordination modulation (CM). Using the CM approach, *in situ* time-resolved SAXS/WAXS experiments and dynamic light scattering (DLS) experiments were carried out for a detailed characterization of the MPA influence on the early stages of nucleation and growth processes. Complementary X-ray photoelectron spectroscopy (XPS) and nitrogen adsorption experiments showed that MPA remains mainly surface confined and adds mesoporosity to the synthesized MOF, thus it can be used for positioning thiol moieties without compromising structural integrity. Moreover, isothermal titration calorimetry (ITC) experiments carried out using the PSM strategy allowed us to determine an enthalpy value of $\sim$7 kJ mol^{-1} associated with the coordination between Zn^{2+} and MPA for the first time to our knowledge.

Design, System, Application

We present a strategy which is useful for both the surface modification and size modulation of metal organic framework porous nanoparticles. The approach is based on colloidal modification and can be applied either through a coordination modulation scheme (*i.e.*, adding a modifying agent together with MOF precursors) or using post-synthetic modification of MOF colloidal suspensions. We were able to determine coordination enthalpies associated with surface coordination for this interesting system. Although the method is discussed thoroughly for a particular MOF class (Zn-based ZIF-8) and a modifying agent (3-mercaptopropionic acid (MPA)), it could be easily adapted to other MOFs and modulators, allowing us to extend thus the range of possible applications in the design of porous films through a top-down strategy. There is a range, however, in which the proposed approach is viable, because the necessary affinity existing between the MOF and modifying agent (in our case, Zn-coordination with carboxylic acid groups of MPA) sets an upper limit of molar ratios possible (and thus the surface density achievable on the modified nanoparticles). If such a limit is exceeded, disassembly of the MOF occurs rather than surface decoration, as discussed in detail.

Introduction

Zeolitic imidazolate frameworks (ZIFs) are a MOF subclass constituted by divalent metallic ions (mainly Zn^{2+} and Co^{2+}) tetrahedrally coordinated with bidentate imidazolate-derived organic linkers. ZIFs feature relatively high thermal and physical stability compared to other common MOFs, and owe their name to the N–M–N coordination bond angle which is very similar to the Si–O–Si covalent bond angle in zeolites.[1,2]

[a] *Instituto de Investigaciones Fisicoquímicas Teóricas y Aplicadas (INIFTA), Fac. de Cs. Exactas, Universidad Nacional de La Plata - CONICET, 64 y Diag. 113, (1900) La Plata, Argentina. E-mail: mrafti@quimica.unlp.edu.ar*
[b] *CIC biomaGUNE, Parque Científico y Tecnologico de Gipuzkoa, Paseo Miramon 182, 20014 Donostia/San Sebastian, Gipuzkoa, Spain*
† Electronic supplementary information (ESI) available. See DOI: 10.1039/d1me00080b

This journal is © The Royal Society of Chemistry and IChemE 2022

Mol. Syst. Des. Eng., 2022, 7, 101–111 | 101

Due to their intrinsic microporosity and high surface areas, MOFs in general (and ZIFs in particular), have triggered intense research activity directed towards exploring possible applications in diverse fields such as adsorption, separations, and heterogeneous catalysis.[3–8] Besides the continuously growing interest in liquid phase applications of MOFs, *e.g.*, drug delivery,[9,10] chromatography[11,12] or sensing and molecular sieving,[13–15] the issue of their stability upon exposure to relevant conditions requires further attention.[16]

ZIF-8 is a characteristic member of ZIF-MOFs (commercially available from BASF Chemical Company as BASOLITE-Z1200®), featuring Zn^{2+} ions tetrahedrally coordinated by the 2-methylimidazolate (MeImH) linker. It features hydrophobic micropores with an 11.6 Å diameter and 3.4 Å pore windows, along with remarkably high nominal BET surface areas ranging from 1500 to 1800 $m^2\ g^{-1}$, depending on synthesis methods and activation procedures followed. Solvothermal approaches for ZIF-8 synthesis have proven to be simple and robust;[17] however, by introducing further modifications from the colloidal chemistry toolbox, a much precise control over size, surface chemistry, and morphology can be attained. For example, both size and shape modulation and surface modification can be accomplished by adding suitable chemical modulators, either together with reactants (coordination modulation, CM) or in a post-synthetic modification (PSM) step.[18–20] The CM approach uses chemical modulation in order to control the formation of coordination bonds during MOF growth,[21,22] while PSM consist in the addition of a modifying agent once the MOF synthesis step is complete, and it was proven useful for the incorporation of desired moieties to the MOF structure.[23]

From the above discussion, the importance of properly addressing the influence of functionalization procedures over the formation mechanisms and stability of MOF nanoparticles is revealed to obtain clear results,[21,24,25] especially if those particles are to be used for the assembly of hierarchical structures such as porous films. In this regard, it was recently shown that the constructional mesoporosity of ZIF-8 films (directly related to the possibility of selective permeation in aqueous environments) can be tuned by careful design of porous nanounits.[26,27] Moreover, it was shown also that such control can be exploited for the design of composite films in which insulating ZIF-8 nanounits and conducting polymers (CPs) are synergically combined. These films were demonstrated to be cost-effective prospective electroactive catalysts with increased efficiency towards the energy relevant oxygen reduction reaction (ORR).[28–30]

Considerable insight can be gained into the early stages of MOF formation by resorting to light scattering techniques, as demonstrated by Cravillon *et al.*,[31,32] who studied room-temperature ZIF-8 synthesis in methanolic solutions. Furthermore, ZIF-8 composites including biologically relevant molecules have been recently studied by Carraro *et al.*,[33] using small angle X-ray scattering. In this work, ZIF-8 particle size control was achieved *via* injection of ethanol into the synthesis mixture. Using high-brilliance synchrotron light sources, small and wide-angle X-ray scattering (SAXS and WAXS) time-resolved experiments allowed scrutinizing even the early stages of relatively fast nucleation processes.[34–37] However, despite the ever-growing number of new MOFs reported, thermodynamic aspects related to MOF synthesis and modification remain relatively unexplored; valuable tools that could be used in order to fill this gap are calorimetric techniques, such as isothermal titration calorimetry (ITC).[38–47]

In this work, important and relatively unexplored thermodynamic aspects of chemical functionalization of MOFs with a modifying agent were explored by resorting to a PSM strategy monitored through an ITC technique.[44–50] Specifically, the enthalpy associated with the MPA modification of ZIF-8 nanounits was determined to be ~7 kJ mol^{-1}. On the other hand, we used the CM approach to study other aspects of the process such as the influence of MPA addition on the formation and growth of ZIF-8 nanounits, which resulted in surface positioning of thiol moieties. In this regard, we present time resolved SAXS and WAXS experiments performed using synchrotron light sources, which allowed a thorough characterization of key features related to the early stages of nucleation and growth processes. Within suitable concentration limits, MPA affects the particle formation kinetics, size polydispersity, and morphology of ZIF-8, while preserving the SOD topology, which is the most stable from the possible polymorphs arising when Zn^{2+} ions and 2-methylimidazole react.[51] The reason behind the election of MPA which features –SH and –COOH moieties is to take advantage of the known affinity between Zn^{2+} and carboxylic acid,[52,53] for the design of size-controlled thiolate-terminated porous colloidal nanounits.[54] These nanounits would then display affinity towards metallic surfaces (*e.g.*, Au, Pt), thus opening a diverse palette for the assembly of monolayers or decoration of diverse metallic nanostructures, adding the interesting feature of porosity.[55,56]

Results of time-resolved experiments suggest that, under the explored conditions, ZIF-8 colloidal formation can be considered as diffusion-controlled.[37,57,58] Furthermore, by analysing the particle size distributions of ZIF-8 and applying the Avrami model, we can rationalize the fact that MPA addition results in larger units, typical of competitive modulation, while XPS measurements allow us to infer that MPA remains mainly surface-confined.

Experimental

Materials

Anhydrous methanol (CH_3OH Anedra, RA-ACS), zinc acetate dihydrate ($ZnC_4H_6O_4 2H_2O$ or $Zn(Ac)_2$ Anedra 99.5%), 2-methylimidazole ($C_4H_6N_2$ or MeImH Aldrich 99%), 3-mercaptopropionic acid ($C_3H_6O_2S$ or MPA Sigma 99%), were used without further purification.

102 | *Mol. Syst. Des. Eng.*, 2022, **7**, 101–111

This journal is © The Royal Society of Chemistry and IChemE 2022

ZIF-8 synthesis and modification with 3-mercaptopropionic acid (MPA)

Methanolic solutions of 25 mM Zn(Ac)$_2$ and 50 mM MeImH were mixed in a 1:1 volumetric proportion (yielding a 1(Zn):2(MeImH):1977(MeOH) molar ratio) and left to react without stirring at room temperature. Both pre- and post-synthetic (*i.e.*, carried out once 90 min synthesis time elapsed) modification procedures were carried out by adding 10 mM MPA 20 µL methanolic stock solution to 2 mL of ZIF-8 synthesis mixture, yielding either (250:1) or (25:1) (MeImH:MPA) molar ratios as discussed below (see further details for molar ratio calculations in the ESI†). In the case of PSM, the MPA and ZIF-8 reaction time was 60 min. All the samples were collected *via* centrifugation (8000 rpm, 30 min) and washed three times with fresh methanol. Since all the procedures followed involve exposure of colloidal suspensions to modifying agents in the methanolic phase, no further activation procedure was carried out (for procedures related to adsorption isotherms, refer to ESI†).

Calorimetric experiments for post-synthetic modification (PSM) of ZIF-8

Isothermal titration calorimetry experiments (ITC) were carried out to characterize the processes occurring during post-synthetic functionalization of ZIF-8 particles with MPA. To this end, colloidal dispersions of 7.9 mM ZIF-8 were used (calculated using a ZIF-8 molar weight of 227.58 ascribed to the stoichiometric relationship between Zn(MeIm)$_2$ and dry weight-derived compositions, see ESI†). Suspensions were placed in a calorimetric cell and appropriate volumes of MPA stock methanolic solutions were added with a micropipette allowing 300 seconds of reaction time. The final molar ratio obtained for (ZIF-8:MPA) was (70:1). The stirring speed and cell temperature were fixed to 394 rpm and 20 °C, respectively.

A MicroCal VP-ITC isothermal titration calorimeter from Malvern was used. The equipment has a pair of coin-shaped cells made of Hastelloy with a 1.456 mL volume. Temperature differences between the reference cell and the sample cell are measured, calibrated to power units. The spin rate range was fixed to 394 rpm and temperature to 293 K. Measurements were run with VP viewer 2000-ITC software.

Small- and wide-angle X-ray scattering (SAXS and WAXS)

SAXS and WAXS experiments were carried out at the SAXS-1 beamline of the Brazilian Synchrotron Light Laboratory (LNLS), Campinas, Brazil. Diffractograms were obtained using a temperature-controlled holder for liquids with two parallel mica windows of 1 mm optical path. The wavelength of the incoming monochromatic X-ray beam was 0.1544 nm. Silver behenate was used for calibration of the sample-to-detector distance (∼3000 mm). A Pilatus 300 K detector (Dectris Ltd., Switzerland) was used to record the scattering patterns. Each individual run was corrected for beam attenuation and time-integrated photon flux following usual procedures. SAXS patterns were modelled using the SASFit

software (version 0.94.6, https://www.psi.ch/en/sinq/sansi/sasfit) in a q range of 0.05–1.34 nm^{-1}. A sphere model with a log-normal distribution of radii was fitted to the experimental data.[59,60] Size distributions are expressed as the polydispersity index, PDI = σ/r, σ being the size distribution standard deviation and r the mean sphere radius. For a typical time-resolved (synchrotron-based) SAXS/WAXS experiment, after fixing the sample–detector distance, the reaction cell was loaded with ZIF-8 precursors. The experimental design allowed a minimum delay between mixing and opening of the X-ray shutter of 35 seconds in every case and given the acquisition period needed for highly diluted samples, 15 seconds was the minimum time resolution achievable.

Dynamic light scattering (DLS)

A Zetasizer Nano ZS apparatus from Malvern was used to determine the nanocrystal colloid size distribution and polydispersity through *in situ* DLS experiments. The temperature of the measurements was 25 °C and the samples were left for 30 seconds for thermalisation. A total of 10 measurements were averaged in the formation and growth characterization of the ZIF-8 and ZIF-8 + MPA $t = 0$ samples.

Scanning and transmission electron microscopy (SEM and TEM)

Images were collected with a FE-SEM SUPRA 40 (Carl Zeiss) without metallization using different magnifications. A LaB6-TEM of type JEOL JEM-1400PLUS (40–120 kV, HC pole piece) equipped with a GATAN US1000 CCD camera (2k × 2k).

X-ray photoelectron spectroscopy (XPS)

Experiments were performed using a SPECS Sage HR 100 spectrometer with a non-monochromatic X-ray source (magnesium Kα line of 1253.6 eV energy and 250 W), placed perpendicular to the analyser axis.

Nitrogen adsorption experiments

Surface area determination was carried using powder samples with an ASAP 2020 HD88 surface area and porosity analyser (Micromeritics). The activation procedure consisted in vacuum drying at 150 °C for 12 h.

Results and discussion

Effect of MPA post-synthetic modification (PSM) on ZIF-8 colloids: determination of suitable concentration ranges

Different conditions were tested for identification of MPA concentration ranges suitable for modification, *i.e.*, a concentration high enough to yield considerable surface functionalization, while not causing degradation of ZIF-8 nanoparticles and loss of the porous crystalline phase. MPA proportions are expressed in terms of MOF linker:modifying agent molar ratios (see ESI† for details). For a MeImH:MPA = 25:1 molar ratio, PSM was observed to cause a gradual

This journal is © The Royal Society of Chemistry and IChemE 2022

Mol. Syst. Des. Eng., 2022, **7**, 101–111 | 103

decrease in the intensity of ZIF-8 diffraction peaks until total disappearance, as monitored *via* WAXS (see Fig. 1). This result can be ascribed to coordinative etching due to the known affinity between the carboxylate moieties of MPA and zinc ions.[52,53] Taking this into account, PSM was then carried out using lower MPA proportions; *i.e.*, we employed a MeImH : MPA = 250 : 1 molar ratio, which was observed to yield the desired surface modification without compromising the ZIF-8 structure, as will be discussed in the next paragraphs. MPA was added then using the PSM strategy to a ZIF-8 colloidal suspension obtained after 1:30 h (90 min.) reaction time (hereafter referred to as ZIF-8 + MPA t = 1:30). Fig. 2(a) shows the SAXS patterns corresponding to the final stage of time evolution for bare ZIF-8 (final size r = 20 nm), and MPA modified. Fig. 2(b) shows the SEM micrographs of nanoparticles obtained using the above-discussed conditions, together with the size distribution (centered at r = 30 nm, comparable to bare ZIF-8 presented in Fig. 4, see below), which provides further support to the results observed in SAXS.

Additionally, the occurrence of further changes upon addition of MPA *via* PSM was investigated *via* N_2 adsorption (see ESI†), TEM (see Fig. S1†) and DLS measurements, together with zeta potential variations (see Fig. S2†). Based on previous reports for similar systems,[26] we hypothesized that the above described PSM approach should lead to the appearance of additional mesoporosity on inherently microporous ZIF-8 units, arising from coordinative etching triggered by affinity between Zn^{2+} and carboxylate moieties. The extent of such modifications can be controlled in principle *via* manipulation of reaction conditions such as temperature, exposure period or modifying agent concentrations. N_2 adsorption isotherms were then measured, and the results obtained for bare and MPA-modified ZIF-8 were compared (see ESI†). Both materials feature type I isotherms corresponding to microporous

materials with comparable BET surface area values (1657 m^2 g^{-1} and 1687 m^2 g^{-1}, for bare and MPA modified materials, respectively), however a hysteresis loop ascribable to the presence of mesopores can be clearly observed only after MPA modification.

Another interesting aspect of MPA used as a modifying agent that can be further scrutinized using the PSM approach is the calorimetric determination of coordination enthalpy values corresponding to the interaction between Zn^{2+} and MPA. To this end, ITC experiments were carried out; Fig. 3 shows the results obtained for PSM ZIF-8 modification using MPA together with the baseline used for deconvolution of multiple operating processes (addition of MPA to bare methanol). MPA coordination is clearly an exothermic process (see Fig. 3) which can be associated with Zn^{2+} ion chelation with carboxylic acid moieties from MPA; however, two possible mechanisms must be considered. Either MPA coordination occurs directly on exposed coordinatively unsaturated Zn^{2+} metal sites (CUS) on the nanoparticle surface, or the process involves instead an additional MeImH linker removal step prior to coordination with MPA (*i.e.*, coordinative etching). This last scenario would generate visible alterations on the otherwise smooth nanoparticle surface, while also be greatly favoured due to the order-loss induced by the exchange between mono (MeImH) and bidentate carboxylate linkers. Removal of the MeIm–Zn coordination bond is an endothermic process with an estimated enthalpy of 12 kJ mol^{-1} in the aqueous phase.[61] The ITC-derived enthalpy value corresponding to MPA coordination was determined to be $\simeq 7$ kJ mol^{-1}, assuming that MPA is the limiting reagent and that there are sufficient sites available for coordination on the nanoparticle surface (see details of calculations in the ESI†). This result can be rationalized by considering the reported values for the enthalpy of Zn^{2+} complexation with acetate ions in the ethanol phase ($\simeq 20$ kJ mol^{-1});[62] as the ITC-determined enthalpy would account for the difference between these processes, ITC results strongly suggest that MPA coordination occurs through replacement of MeIm-Zn *via* coordinative etching ($\simeq 8$ kJ mol^{-1}) rather than direct coordination with Zn^{2+} CUS.[62,63]

Particle size and crystalline structure temporal evolution of ZIF-8 when using coordination modulation with MPA

Having determined the suitable MPA concentration ranges for ZIF-8 stability *via* the PSM experiments described above, we employed such conditions to assess the influence of MPA as a coordination modulator (CM). SAXS experiments were carried out during colloidal synthesis of ZIF-8 following the same procedures as those discussed above. The obtained time-dependent scattering patterns were modelled assuming hard spheres and log-normal size distributions, as shown in Fig. 4a) and b) (see the Experimental section for details). For the earliest experimentally accessible time interval (~30 s) objects of radius $r \approx 17$ nm were detected, which then
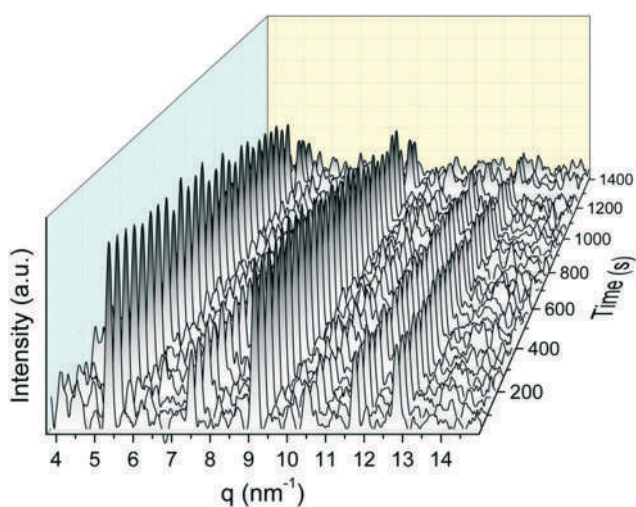

Fig. 1 Time evolution obtained *via* WAXS for ZIF-8 colloidal suspensions upon addition of MPA for a final (25 : 1) molar ratio.[1]
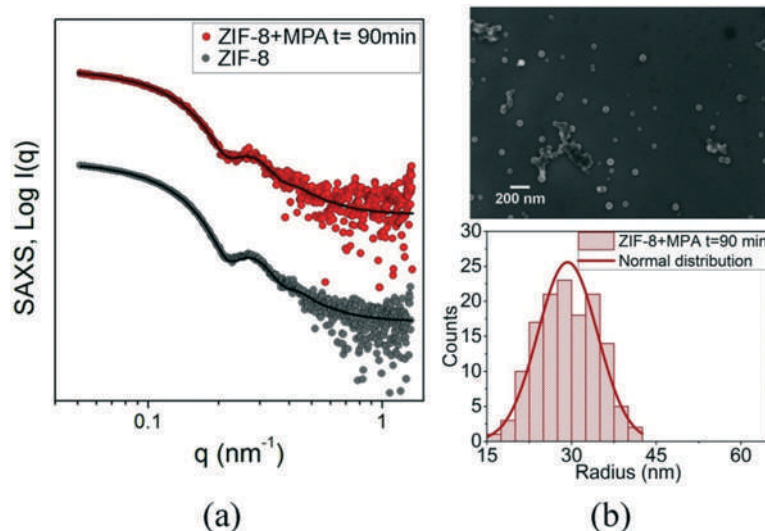
Fig. 2 (a) SAXS scattering pattern of the final state of ZIF-8 + MPA t = 90 min. Data were fit using a sphere model. (b) SEM images and its corresponding size distribution. Differences in sizes compared to the SAXS radius are related to different size estimation from each technique.
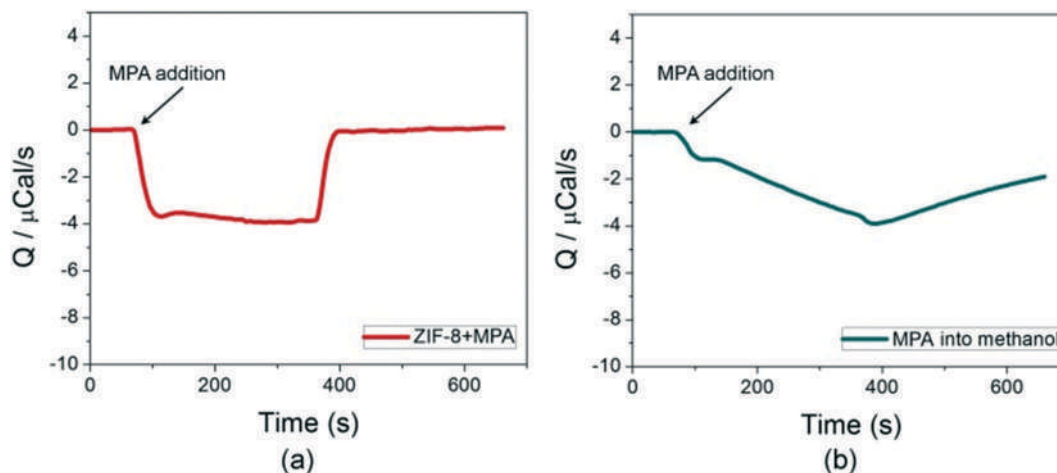

Fig. 3 (a) ITC thermograms of ZIF-8 during the MPA reaction (1111 μJ total energy for ZIF-8 + MPA). (b) Calorimetric curve of MPA in methanol, whose total energy is −5416 μJ. This value was subtracted to (a).[6]

gradually increased in size until reaching a limit value of $r \approx$ 26 nm for 400–500 seconds, featuring relatively low polydispersity (PDI ∼ 0.11). As shown in Fig. 4b), the PDI reduction profile matches with the theoretical predictions corresponding to a diffusion-controlled process.[37,57,58] In order to determine the real-time evolution of the crystalline structure of nanoparticles obtained, growth processes were also monitored *in situ via* WAXS. The observed features correspond to typical ZIF-8 SOD phase diffraction peaks, and allows confirmation on the identity of the material obtained (see Fig. 4c) and d)). The time evolution of the ZIF-8 crystallization extent (α) is also shown as the inset in Fig. 4c), which was calculated taking as a reference the area of the diffraction peak centered at q = 5.25 nm^{-1} corresponding to the (110) ZIF-8 crystallographic plane.

For experiments including MPA together with ZIF-8 precursors for a fixed molar ratio 250 : 1 of MeImH : MPA, the product obtained will be hereafter referred to as ZIF-8 + MPA t = 0 (*i.e.*, CM approach). Time-dependent SAXS patterns show a remarkably low polydispersity, as evidenced by the local minima observed (at q ∼ 0.15 nm^{-1}) in the scattering patterns readily detectable for t > 45 s. (see Fig. 5). The derived size evolution presented in Fig. 5 is similar to what was obtained for bare ZIF-8 in Fig. 4; however, the final nanocrystal size ($r \approx$ 40 nm) is 60% larger. ESI† Fig. S3 shows a comparison of WAXS experiments carried out in order to demonstrate that the crystalline structure of bare ZIF-8 and ZIF-8 + MPA t = 0 is consistent with the calculated diffractograms.[2] Reproducibility of the above-discussed SAXS results was confirmed by carrying out additional dynamic

View Article Online

Paper   MSDE
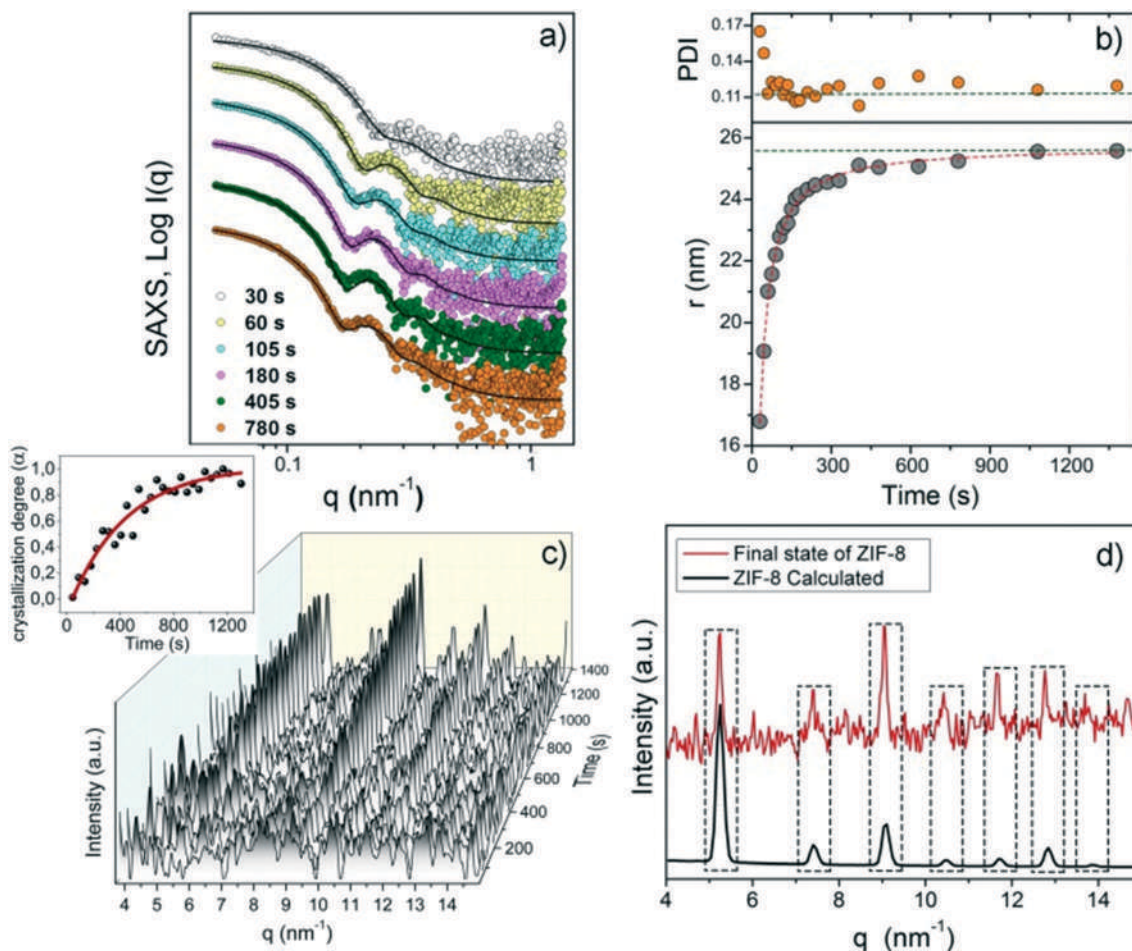
Fig. 4 a) Time evolution of the SAXS scattering patterns of ZIF-8, solid lines represent the best fit obtained using the hard sphere model and log-normal size distribution (see text). b) Size distribution (lower panel) and polydispersity index (PDI = σ/r (σ, standard deviation) upper panel). c) Time evolution of WAXS patterns. The inset shows the crystallization extent evolution of ZIF-8 SOD crystals as calculated from the increasing relative area of (110) reflection. The red line is the best fit obtained using a hyperbolic function. d) WAXS pattern of ZIF-8 SOD nanoparticles obtained for the final state of synthesis.

light scattering (DLS) experiments, which although imposing some limitations on the accessible time scale due to the extended collection periods needed, allow us to confirm the previously described results. Fig. S4 in the ESI† shows the DLS-derived temporal size evolution of both ZIF-8 and ZIF-8 + MPA $t = 0$, which is in line with SAXS observations. SEM micrographs and size distribution analysis also confirm the effect of MPA addition as can be observed in Fig. 6. For ZIF-8 synthesis, nanocrystals with a size distribution centered around 35 nm were obtained, while for ZIF-8 + MPA $t = 0$ the size distribution is centered around 45 nm.

Using the SAXS and DLS time-resolved experimental data obtained and empirical models for nucleation (see eqn (S1)–(S3) in the ESI†) allows gaining further insight into the underlying operating growth mechanism. As shown in Fig. S5–S6 and Table S1 (see ESI†), and based on the maximum R^2 regression coefficient, the growth process for the hereby explored conditions is compatible with a diffusion-controlled mechanism. It should be stressed that numerical values obtained for specific model parameters are not meant to be

exhaustive due to the wide variety of ZIF-8 synthesis methods and conditions described in the literature. However, as methanolic solutions of precursors and room temperature are among the most used conditions, hereby the reported parameter values are of great significance. On the same note, DLS and SAXS are based on different principles and employ distinct approximations, therefore, minor discrepancies are to be expected.

In order to rationalize the size increase caused by MPA addition, SAXS results were fitted within the framework of the classical Avrami model ($\alpha = 1 - e^{-kt}$), where $\alpha = r/R$ is determined as the ratio of the time-dependent radius $r(t)$ and final radius R, t represents the reaction time, and k is the reaction rate constant. Fig. 7 shows the data fitting obtained using the Sharp–Hancock method,[64] numerical results are summarized in Table 1.

Linear fitting of data corresponding to the ZIF-8 size time evolution features an Avrami exponent value of $n = 0.43$, which suggests a diffusion-limited process.[37,57,58] On the other hand, ZIF-8 + MPA $t = 0$ experiments can be fitted more

106 | *Mol. Syst. Des. Eng.*, 2022, **7**, 101–111

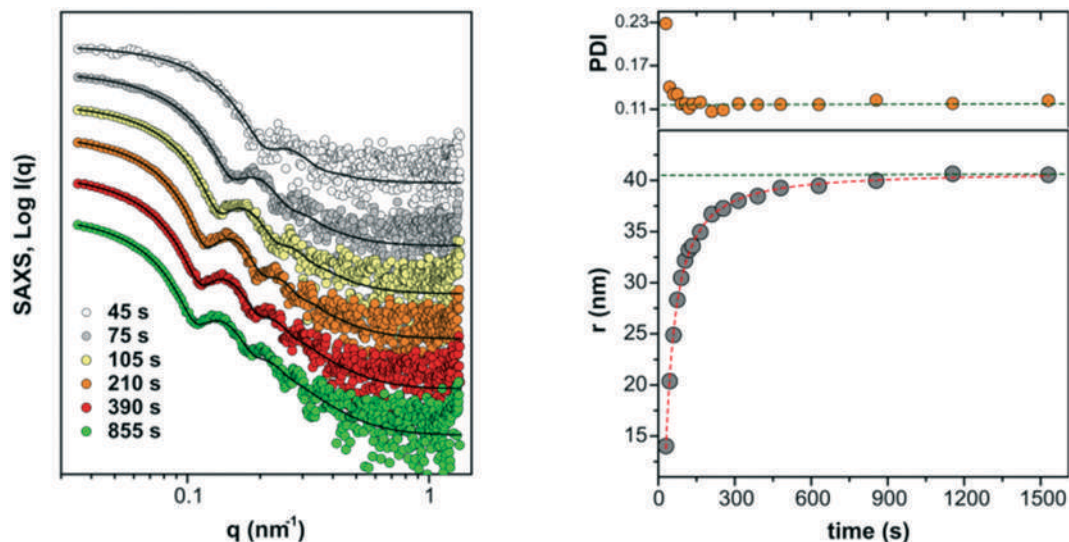This journal is © The Royal Society of Chemistry and IChemE 2022

Fig. 5 (left panel) Time evolution of SAXS scattering patterns for the MPA modified ZIF-8 synthesis (ZIF-8 + MPA $t = 0$), solid lines represent the best fit obtained using the hard sphere model and log-normal size distribution (see text). (right panel) Size evolution (bottom) and polydispersity index (PDI = σ/r (σ, standard deviation), top).[3]
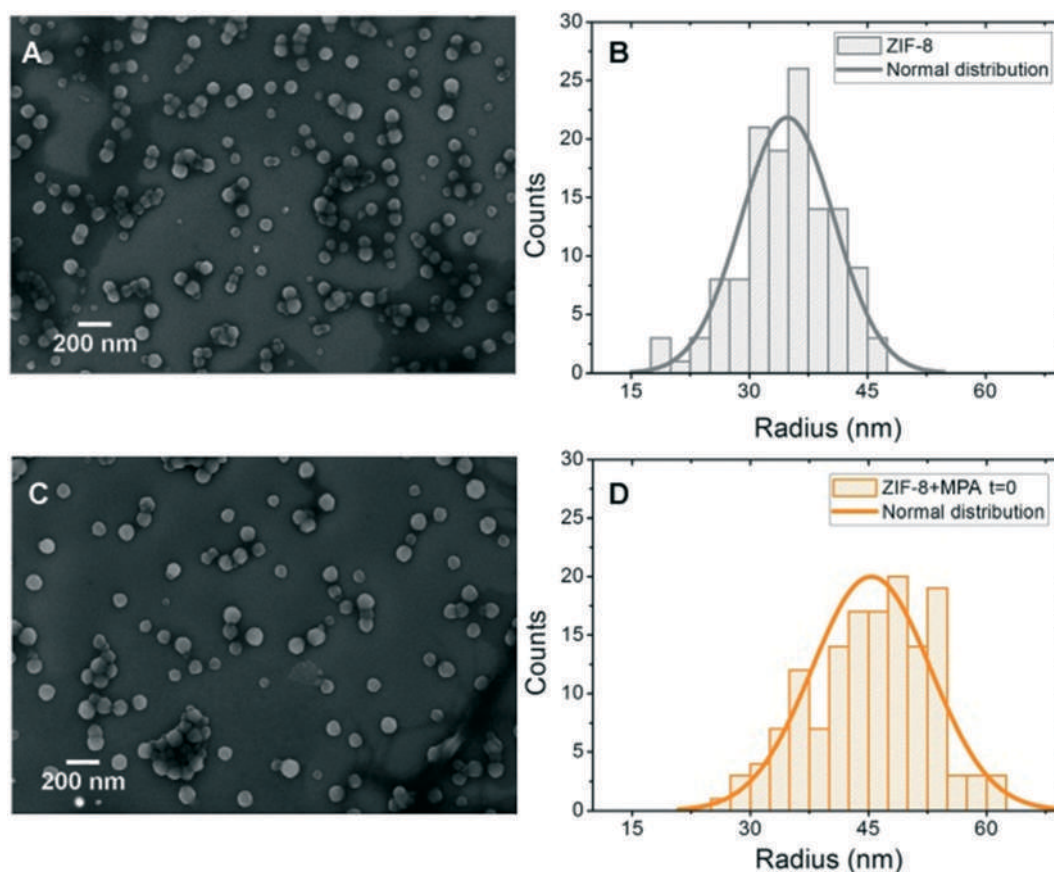

Fig. 6 SEM micrographs of (A) ZIF-8 and (B) ZIF-8 + MPA $t = 0$ and their corresponding size distribution (C) and (D) respectively. Trends are similar to SAXS results, despite differences in sizes compared to the SAXS radius related to different size estimation from each technique.[2]

appropriately by assuming two regimes operating in subsequent stages: a phase boundary growth process for an initial stage ($n = 0.95$),[22] followed by a diffusion-limited process ($n = 0.46$). Differences observed can be understood by
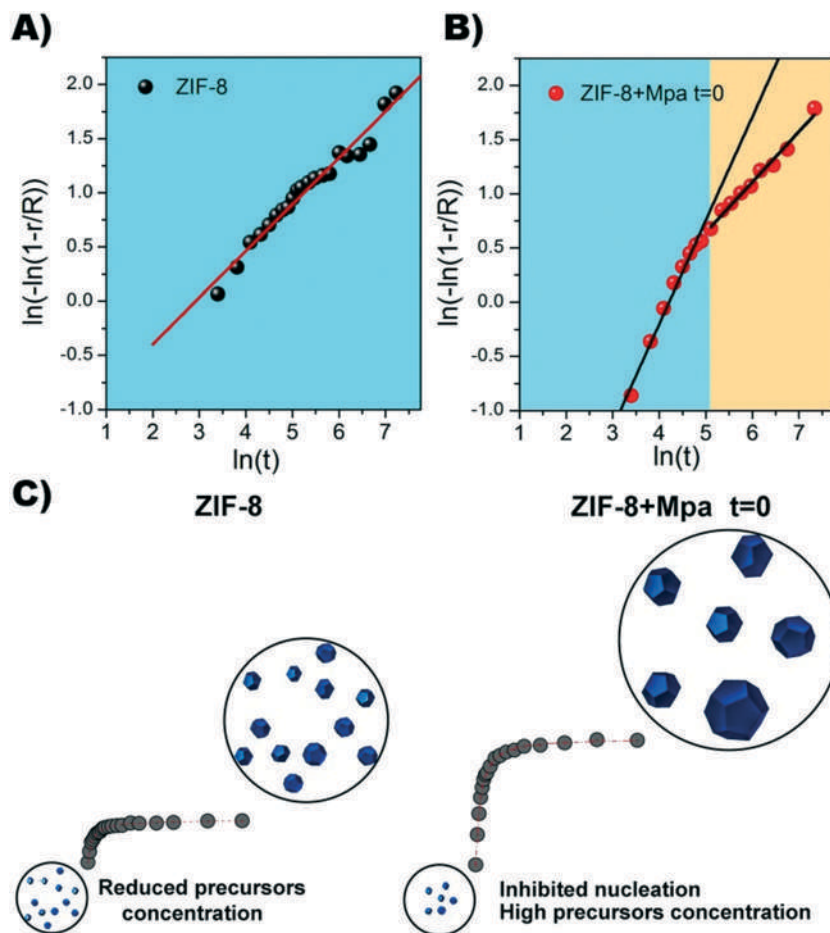
Fig. 7 Avrami analysis of the data obtained from the SAXS growth profiles. A) ZIF-8 and B) ZIF-8 + MPA $t = 0$. The variable r is the radius of the particle depending on the time ($r_{(t)}$) and R is the final radius reached by each system. C) Comparison of the formation and growth mechanism proposed for ZIF-8 and ZIF-8 + MPA $t = 0$ colloidal suspensions. The grey points represent the size evolution of the nanocrystals.[4]

resorting to several facts. Firstly, the reduction of the crystallization rate constant observed for MPA addition in the CM scheme (see Table 1) can be rationalized by taking into account that MPA might suppress deprotonation of MeImH, which is in turn necessary for ZIF-8 formation steps ($[Zn(MeIm)_x(MeImH)_y(L)_z]$ intermediate complexes, where L represents the additional coordinating linkers subject to further exchange reactions).[65] Secondly, due to a larger alkyl chain, formation of carboxylic acid-mediated Zn^{2+}–MPA complexes is favoured with respect to acetate complexes,[52]

and thus leads to a decreased number of condensation events leading to formation of ZIF-8 nuclei with sizes above the critical radius.[65] Such a decreased number of nuclei would explain the observed larger final radius in ZIF-8 + MPA $t = 0$ experiments due to a higher concentration of free precursors, in line also with the fitting parameters obtained typical of competitive modulation (see scheme in Fig. 7C)).[32,66]

Having established the role of MPA as a modulator in ZIF-8 nucleation and growth processes, XPS experiments were carried out to determine the surface composition of nanoparticles (see Fig. 8). A signal centered at a BE of approx. 165–167 eV ascribable to the presence of S ($2p_{3/2}$) can be observed in Fig. 8(b), suggesting the presence of thiol-terminated moieties (see comparison between experimentally obtained S : Zn% proportions and calculations in Table S2†). In addition, we have recently found similar results with thiol-functionalized ZIF-8 nanocrystals using cysteamine as a functionalizing agent.[26]

Conclusions

In this work we explored both PSM and CM approaches towards ZIF-8 synthesis using MPA as a chemical modifying

Table 1 Fitting parameters of the Avrami analysis obtained for different crystallization temporal domains of ZIF-8 and ZIF-8 + MPA $t = 0$. n is the Avrami exponent, k is the crystallization rate constant, and $t_{ind} = 1/k$ is the induction time

	ZIF-8	ZIF-8 + MPA $t = 0$	
		First time interval	Second time interval
n	0.43 ± 0.01	0.95 ± 0.05	0.46 ± 0.02
$n \ln k$	-1.25 ± 0.09	-4.0 ± 0.2	-1.6 ± 0.1
k (s^{-1})	0.05 ± 0.01	0.014 ± 0.004	0.026 ± 0.008
t_{ind} (s)	18.6 ± 4	67 ± 20	37 ± 11
R^2	0.9702	0.9821	0.9864

108 | *Mol. Syst. Des. Eng.*, 2022, **7**, 101–111

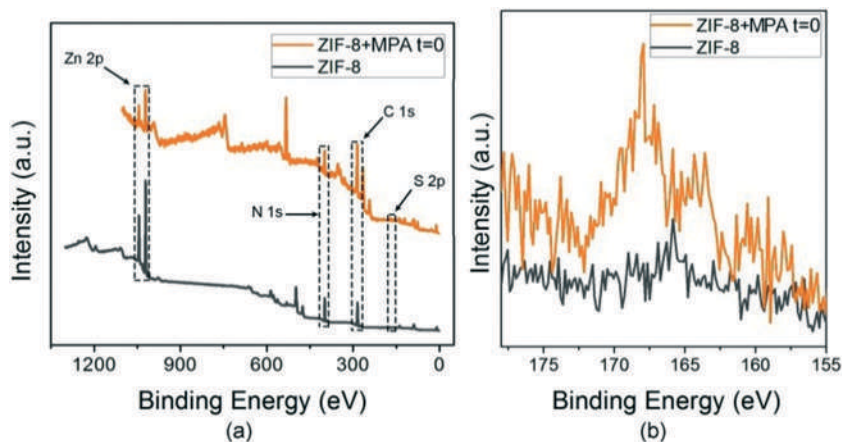This journal is © The Royal Society of Chemistry and IChemE 2022

Fig. 8 (a) XPS survey spectra of ZIF-8 and ZIF-8 + MPA t = 0 samples and (b) XPS spectra of the energy region of S 2p for ZIF-8 (gray) and ZIF-8 + MPA t = 0 (orange).[5]

agent. The concentration ranges used were constrained to cause observable surface modification, while still preserving the MOF crystalline structure. By resorting to time resolved experiments using a CM synthesis approach, we were able to determine the occurrence of a size modulation effect due to competition for Zn^{2+} ions between MeImH and MPA. ZIF-8 formation and growth were observed to follow a diffusion-controlled mechanism while addition of MPA was observed to make the process phase-boundary limited instead. For determining enthalpies corresponding to MPA and Zn^{2+} coordination, we resorted to a PSM synthesis scheme, and were able to identify the operating mechanism and an approximate value for coordination enthalpy.

In summary, MPA modification was shown to constitute a feasible way to synthesize thiol-decorated ZIF-8 nanounits with reduced polydispersity, and preserved both the surface area and crystalline structure. Therefore, we consider that this is a promising strategy for the design of porous (both micro and meso) colloidal building blocks with tailored affinity towards metallic surfaces, with multiple possibilities in the design of functional nanoarchitectures.[26,54]

Conflicts of interest

There are no conflicts to declare.

Acknowledgements

Notes and references

1 B. Wang, A. P. Côté, H. Furukawa, M. O'Keeffe and O. M. Yaghi, *Nature*, 2008, **453**, 207–211.

2 K. S. Park, Z. Ni, A. P. Côté, J. Y. Choi, R. Huang, F. J. Uribe-Romo, H. K. Chae, M. O'Keeffe and O. M. Yaghi, *Proc. Natl. Acad. Sci. U. S. A.*, 2006, **103**, 10186–10191.

3 S. Tanaka, K. Fujita, Y. Miyake, M. Miyamoto, Y. Hasegawa, T. Makino, S. Van Der Perre, J. Cousin Saint Remi, T. Van Assche, G. V. Baron and J. F. M. Denayer, *J. Phys. Chem. C*, 2015, **119**, 28430–28439.

4 N. C. Burtch, H. Jasuja and K. S. Walton, *Chem. Rev.*, 2014, **114**, 10575–10612.

5 H. Furukawa, K. E. Cordova, M. O'Keeffe and O. M. Yaghi, *Science*, 2013, **341**, 1230444.

6 T. R. Cook, Y. R. Zheng and P. J. Stang, *Chem. Rev.*, 2013, **113**, 734–777.

7 G. Férey, *Chem. Soc. Rev.*, 2008, **37**, 191–214.

8 E. Stavitski, M. Goesten, J. Juan-Alcañiz, A. Martinez-Joaristi, P. Serra-Crespo, A. V. Petukhov, J. Gascon and F. Kapteijn, *Angew. Chem., Int. Ed.*, 2011, **50**, 9624–9628.

9 P. Horcajada, T. Chalati, C. Serre, B. Gillet, C. Sebrie, T. Baati, J. F. Eubank, D. Heurtaux, P. Clayette, C. Kreuz, J.-S. Chang, Y. K. Hwang, V. Marsaud, P.-N. Bories, L. Cynober, S. Gil, G. Férey, P. Couvreur and R. Gref, *Nat. Mater.*, 2010, **9**, 172–178.

10 J. G. Yañuk, M. L. Alomar, M. M. Gonzalez, F. Simon, R. Erra-Balsells, M. Rafti and F. M. Cabrerizo, *Phys. Chem. Chem. Phys.*, 2015, **17**, 12462–12465.

11 R. Ahmad, A. G. Wong-Foy and A. J. Matzger, *Langmuir*, 2009, **25**, 11977–11979.

12 N. Mizutani, N. Hosono, B. Le Ouay, T. Kitao, R. Matsuura, T. Kubo and T. Uemura, *J. Am. Chem. Soc.*, 2020, **142**, 3701–3705.

13 D. Zacher, O. Shekhah, C. Wöll and R. A. Fischer, *Chem. Soc. Rev.*, 2009, **38**, 1418.

14 B. Liu, M. Tu and R. A. Fischer, *Angew. Chem., Int. Ed.*, 2013, **52**, 3402–3405.

This journal is © The Royal Society of Chemistry and IChemE 2022

Mol. Syst. Des. Eng., 2022, **7**, 101–111 | 109

15 J. Yao, D. Dong, D. Li, L. He, G. Xu and H. Wang, *Chem. Commun.*, 2011, **47**, 2559–2561.

16 K. A. Cychosz and A. J. Matzger, *Langmuir*, 2010, **26**, 17198–17202.

17 H. C. Zhou, J. R. Long and O. M. Yaghi, *Chem. Rev.*, 2012, **112**, 673–674.

18 M. Sindoro, N. Yanai, A. Y. Jee and S. Granick, *Acc. Chem. Res.*, 2014, **47**, 459–469.

19 A. Umemura, S. Diring, S. Furukawa, H. Uehara, T. Tsuruoka and S. Kitagawa, *J. Am. Chem. Soc.*, 2011, **133**, 15506–15513.

20 N. Yanai and S. Granick, *Angew. Chem., Int. Ed.*, 2012, **51**, 5638–5641.

21 S. Diring, S. Furukawa, Y. Takashima, T. Tsuruoka and S. Kitagawa, *Chem. Mater.*, 2010, **22**, 4531–4538.

22 J. Cravillon, C. A. Schröder, H. Bux, A. Rothkirch, J. Caro and M. Wiebcke, *CrystEngComm*, 2012, **14**, 492–498.

23 Y. Yoo and H. K. Jeong, *Chem. Eng. J.*, 2012, **181–182**, 740–745.

24 G. Zahn, P. Zerner, J. Lippke, F. L. Kempf, S. Lilienthal, C. A. Schröder, A. M. Schneider and P. Behrens, *CrystEngComm*, 2014, **16**, 9198–9207.

25 T. Tsuruoka, S. Furukawa, Y. Takashima, K. Yoshida, S. Isoda and S. Kitagawa, *Angew. Chem., Int. Ed.*, 2009, **48**, 4739–4743.

26 G. M. Segovia, J. S. Tuninetti, O. Azzaroni and M. Rafti, *ACS Appl. Nano Mater.*, 2020, **3**, 11266–11273.

27 J. S. Tuninetti, M. Rafti, A. Andrieu-Brunsen and O. Azzaroni, *Microporous Mesoporous Mater.*, 2016, **220**, 253–257.

28 A. P. Mártire, G. M. Segovia, O. Azzaroni, M. Rafti and W. Marmisollé, *Mol. Syst. Des. Eng.*, 2019, **4**, 893–900.

29 G. E. Fenoy, J. Scotto, J. Azcárate, M. Rafti, W. A. Marmisollé and O. Azzaroni, *ACS Appl. Energy Mater.*, 2018, **1**, 5428–5436.

30 M. Rafti, W. A. Marmisollé and O. Azzaroni, *Adv. Mater. Interfaces*, 2016, **3**, 1–5.

31 J. Cravillon, S. Münzer, S. J. Lohmeier, A. Feldhoff, K. Huber and M. Wiebcke, *Chem. Mater.*, 2009, **21**, 1410–1412.

32 J. Cravillon, R. Nayuk, S. Springer, A. Feldhoff, K. Huber and M. Wiebcke, *Chem. Mater.*, 2011, **23**, 2130–2141.

33 F. Carraro, J. D. Williams, M. Linares-Moreau, C. Parise, W. Liang, H. Amenitsch, C. Doonan, C. O. Kappe and P. Falcaro, *Angew. Chem.*, 2020, **132**, 8200–8204.

34 X. Chen, J. Schröder, S. Hauschild, S. Rosenfeldt, M. Dulle and S. Förster, *Langmuir*, 2015, **31**, 11678–11691.

35 C. S. Tsao, M. S. Yu, T. Y. Chung, H. C. Wu, C. Y. Wang, K. Sen Chang and H. L. Chen, *J. Am. Chem. Soc.*, 2007, **129**, 15997–16004.

36 R. Nayuk, D. Zacher, R. Schweins, C. Wiktor, R. A. Fischer, G. Van Tendeloo and K. Huber, *J. Phys. Chem. C*, 2012, **116**, 6127–6135.

37 J. Cravillon, C. A. Schröder, R. Nayuk, J. Gummel, K. Huber and M. Wiebcke, *Angew. Chem., Int. Ed.*, 2011, **50**, 8067–8071.

38 J. T. Hughes and A. Navrotsky, *J. Am. Chem. Soc.*, 2011, **133**, 9184–9187.

39 J. T. Hughes, T. D. Bennett, A. K. Cheetham and A. Navrotsky, *J. Am. Chem. Soc.*, 2013, **135**, 598–601.

40 C. Zhou, M. Stepniewska, L. Longley, C. W. Ashling, P. A. Chater, D. A. Keen, T. D. Bennett and Y. Yue, *Phys. Chem. Chem. Phys.*, 2018, **20**, 18291–18296.

41 J. T. Hughes, D. F. Sava, T. M. Nenoff and A. Navrotsky, *J. Am. Chem. Soc.*, 2013, **135**, 16256–16259.

42 D. Wu, J. J. Gassensmith, D. Gouveîa, S. Ushakov, J. F. Stoddart and A. Navrotsky, *J. Am. Chem. Soc.*, 2013, **135**, 6790–6793.

43 I. J. Bruno, J. C. Cole, P. R. Edgington, M. Kessler, C. F. Macrae, P. McCabe, J. Pearson and R. Taylor, *Acta Crystallogr., Sect. B: Struct. Sci.*, 2002, **58**, 389–397.

44 D. Wu and A. Navrotsky, *J. Solid State Chem.*, 2015, **223**, 53–58.

45 Z. Akimbekov and A. Navrotsky, *ChemPhysChem*, 2016, **17**, 468–470.

46 M. Arhangelskis, A. D. Katsenis, N. Novendra, Z. Akimbekov, D. Gandrath, J. M. Marrett, G. Ayoub, A. J. Morris, O. K. Farha, T. Friščić and A. Navrotsky, *Chem. Mater.*, 2019, **31**, 3777–3783.

47 H. Sun and D. Wu, *Powder Diffr.*, 2019, **34**, 297–301.

48 V. Agostoni, R. Anand, S. Monti, S. Hall, G. Maurin, P. Horcajada, C. Serre, K. Bouchemal and R. Gref, *J. Mater. Chem. B*, 2013, **1**, 4231–4242.

49 A. Aykaç, M. Noiray, M. Malanga, V. Agostoni, J. M. Casas-Solvas, É. Fenyvesi, R. Gref and A. Vargas-Berenguel, *Biochim. Biophys. Acta, Gen. Subj.*, 2017, **1861**, 1606–1616.

50 R. J. Drout, S. Kato, H. Chen, F. A. Son, K. I. Otake, T. Islamoglu, R. Q. Snurr and O. K. Farha, *J. Am. Chem. Soc.*, 2020, **142**, 12357–12366.

51 Y. Lo, C. H. Lam, C. W. Chang, A. C. Yang and D. Y. Kang, *RSC Adv.*, 2016, **6**, 89148–89156.

52 A. Bujak, I. Filipović, B. Mayer, I. Piljac, B. Bach-Dragutinović and T. Matusinović, *Croat. Chem. Acta*, 1971, **42**, 541–549.

53 S. Bagchi, D. Mandal, D. Ghosh and A. K. Das, *J. Phys. Chem. A*, 2013, **117**, 1601–1613.

54 G. M. Segovia, J. S. Tuninetti, S. Moya, A. S. Picco, M. R. Ceolín, O. Azzaroni and M. Rafti, *Mater. Today Chem.*, 2018, **8**, 29–35.

55 D. Esken, S. Turner, O. I. Lebedev, G. Van Tendeloo and R. A. Fischer, *Chem. Mater.*, 2010, **22**, 6393–6401.

56 C. V. McGuire and R. S. Forgan, *Chem. Commun.*, 2015, **51**, 5199–5217.

57 A. Polyzoidis, M. Etter, M. Herrmann, S. Loebbecke and R. E. Dinnebier, *Inorg. Chem.*, 2017, **56**, 5489–5492.

58 N. T. K. Thanh, N. Maclean and S. Mahiddine, *Chem. Rev.*, 2014, **114**, 7610–7630.

59 I. Breßler, J. Kohlbrecher and A. F. Thünemann, *J. Appl. Crystallogr.*, 2015, **48**, 1587–1598.

60 A. Guinier and G. Fournet, *Small-Angle Scattering of X-Rays*, John Wiley and Sons, Inc., New York, NY, 1955.

61 Y. Nozaki, F. R. N. Gurd, R. F. Chen, J. T. Edsall, Y. Nozaki, F. R. N. Gurd, R. F. Chen and J. T. Edsall, *J. Am. Chem. Soc.*, 1957, **79**, 2123–2129.

62 N. Rodríguez-Laguna, L. I. Reyes-García, R. Pacheco-Gómez, R. Flores, A. Rojas-Hernández and R. Gómez-Balderas, *J. Therm. Anal. Calorim.*, 2019, **136**, 1701–1709.

63 Ü. Kökçam-Demir, A. Goldman, L. Esrafili, M. Gharib, A. Morsali, O. Weingart and C. Janiak, *Chem. Soc. Rev.*, 2020, **49**, 2751–2798.

64 J. D. Hancock and J. H. Sharp, *J. Am. Ceram. Soc.*, 1972, **55**, 74–77.

65 H. H.-M. Yeung, A. F. Sapnik, F. Massingberd-Mundy, M. W. Gaultois, Y. Wu, D. A. X. Fraser, S. Henke, R. Pallach, N. Heidenreich, O. V. Magdysyuk, N. T. Vo and A. L. Goodwin, *Angew. Chem.*, 2018, 576–581.

66 M. Goesten, E. Stavitski, E. A. Pidko, C. Gücüyener, B. Boshuizen, S. N. Ehrlich, E. J. M. Hensen, F. Kapteijn and J. Gascon, *Chem. – Eur. J.*, 2013, **19**, 7809–7816.

This journal is © The Royal Society of Chemistry and IChemE 2022

Mol. Syst. Des. Eng., 2022, **7**, 101–111 | **111**